Salt-Mediated Self-Assembly of Thioctic Acid on Gold Nanoparticles

Anna A. Volkert,† Varuni Subramaniam,† Michael R. Ivanov, Amanda M. Goodman, and Amanda J. Haes*

Department of Chemistry, University of Iowa, Iowa City, Iowa 52242, United States. †Contributed equally.

ABSTRACT Self-assembled monolayer (SAM) modification is a widely used method to improve the functionality and stability of bulk and nanoscale materials. For instance, the chemical compatibility and utility of solution-phase nanoparticles are often improved using covalently bound SAMs. Herein, solution-phase gold nanoparticles are modified with thioctic acid SAMs in the presence and absence of salt. Molecular packing density on the nanoparticle surfaces is estimated using X-ray photoelectron spectroscopy and increases by ~20% when molecular self-assembly occurs in the presence *versus* the absence of salt. We hypothesize that as the ionic strength of the solution increases, pinhole and collapsed-site defects in the SAM are more easily accessible as the electrostatic interaction energy between adjacent molecules decreases, thereby facilitating the subsequent assembly of additional thioctic acid molecules. Significantly, increased SAM packing densities increase the stability of functionalized gold nanoparticles by a factor of 2 relative to nanoparticles functionalized in the absence of salt. These results are expected to improve the reproducible functionalization of solution-phase nanomaterials for various applications.

KEYWORDS: gold nanoparticles · self-assembled monolayers · thioctic acid · nanoparticle stability

Surface modification via self-assembled monolayers (SAMs) is revolutionizing how surfaces and interfaces are modified for applications in biosensors, biotechnology, chemical sensors, and molecular electronics.[1−12] A wide variety of ligands (*i.e.*, amine, carboxylate, isocyanide, phosphine, and thiol)[13−18] form SAMs on gold films[1] and colloidal particles;[5,19−24] however, thiol/disulfide surface attachment groups are widely employed because of the strong bond that forms between gold and sulfur.[1] Self-assembly of alkanethiols onto a metal surface can occur in either organic[4,6,13] or aqueous[17,25,26] phases, with the latter being predominate for solution-phase nanoparticles with diameters greater than 10 nm.[12,24,27] In all cases, the stability of solution-phase nanoparticles can be improved with SAMs, thereby increasing their usefulness in biology, catalysis, and nanotechnology.[5,22,25−41]

Predictable utilization of thiol-functionalized gold nanoparticles in any application relies on the reproducible assembly of SAMs on their surfaces. Alkanethiol chains composed of more than 10 carbon atoms produce SAMs that are more highly ordered and oriented with increased molecular packing densities than shorter chains.[42,43] These SAMs, however, generally contain at least three types of defect sites: pinholes, gauche defects in alkyl chains,[44] and collapsed-site defects which arise from (1) imperfect adsorption of alkanethiols during the self-assembly process, (2) thermally and tilt-order driven chain dynamics, and/or (3) loss of thiols during rinsing, storage, and use.[42,45] For thiols on flat gold surfaces, the fraction of these defect sites to the total surface area is estimated at ~5−10%.[46−48] While the influence of alkanethiol chain length, anchoring group, chemical composition, immersion time, and substrate topography was previously investigated for nanoparticles,[42,49−51] no evaluation of defect sites on solution-phase nanoparticles and implications thereof was performed.

In these studies, we investigate how the ionic strength of the dielectric medium impacts the self-assembly of thioctic acid on the surface of gold nanoparticles. Specifically, an increase in NaCl concentration during alkanethiol incubation increases the packing density of thioctic acid SAMs on gold nanoparticles by 17%, while their stability increases by approximately the same magnitude *versus* control studies. During SAM modification, the core size and optical properties of the gold nanoparticles will be shown to remain statistically unchanged as revealed by transmission electron microscopy (TEM) and extinction spectroscopy, respectively. In contrast, zeta potential and X-ray photoelectron spectroscopy (XPS) will reveal that the effective surface charge and sulfur to gold atomic ratio of functionalized gold nanoparticles, respectively, vary systematically then saturate as the estimated SAM packing density equilibrates. Estimations of the ionic strength dependent electrostatic interaction energy between carboxylic acid terminal groups in

* Address correspondence to amanda-haes@uiowa.edu.

Received for review January 22, 2011 and accepted April 27, 2011.

Published online April 27, 2011
10.1021/nn200276a

the SAM provide a rational explanation for these experimental observations. Significantly, nanoparticles functionalized in the presence of salt will be shown to be approximately twice as stable as nanoparticles prepared in the absence of salt. These data support that SAM packing density increases as a function of increasing NaCl concentration, thereby suggesting that the density of pinhole and/or collapsed-site defects on nanoparticle surfaces is reduced. Better control in alkanethiol packing density as a result of a salt-mediated SAM assembly on gold nanoparticles will be fundamental in achieving reproducible gold nanoparticle covalent functionalization and their subsequent utility in applications and new technologies.

RESULTS AND DISCUSSION

Structural Characterization of Thioctic Acid Functionalized Au Nanoparticles. Figure 1 depicts the self-assembly of thioctic acid on gold (Au@TA) nanoparticles. After initially functionalizing these nanostructures with thioctic acid and allowing them to incubate for 16 h, NaCl is added incrementally in 8 h incubation steps to promote thioctic acid self-assembly. Au@TA nanoparticles remain stable up to 16 mM salt concentrations. Above this concentration, Au@TA nanoparticles begin to aggregate, as indicated by the growth of a characteristic low-energy (~620 nm) extinction band (data not shown). Because each salt-containing gold nanoparticle aliquot was allowed to incubate for 8 h, time control assays (*i.e.*, equal incubation times in the absence of salt) are included. Structural analysis of these nanostructures *via* TEM reveals that average nanoparticle size does not change significantly throughout the SAM formation process (in the presence or the absence of salt) (Figure S1). A representative TEM image of Au@TA nanostructures is shown in Figure 1B. As expected, Au@TA nanoparticles are spherical and exhibit a mean diameter of $11.6_1 \pm 0.9_8$ nm.

Noble metal nanoparticles (copper, gold, silver, *etc.*) exhibit strong extinction properties in the visible region of the electromagnetic spectrum,[52−59] which are sensitive to changes in nanoparticle shape, size, stability, and local dielectric constant (*i.e.*, the surrounding medium and/or surface modifications).[60,61] Localized surface plasmon resonance (LSPR) spectra arise when the incident photon frequency is in resonance with the collective oscillation of the conduction electrons in the nanoparticles.[62] Figure 1D shows the LSPR spectra of citrate-stabilized gold (Au@citrate) (0 h) and Au@TA nanoparticles after being functionalized in thioctic acid at varying salt concentrations. To ensure that bulk refractive index changes are not impacting these sensitive optical properties, the nanoparticles were washed and redispersed in 20 mM borate buffer (pH 9) prior to each measurement. The gold nanoparticles exhibit an extinction maximum (λ_{max}) at ~518 prior to

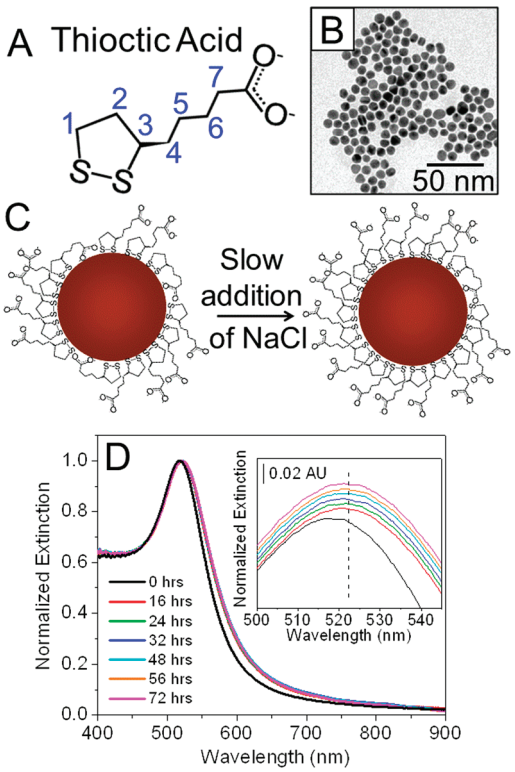

Figure 1. Slow addition of NaCl to Au@TA nanoparticles. (A) Structure and proton assignments used for thioctic acid. (B) Representative TEM image of Au@TA nanoparticles (average diameter, $d = 11.6_1 \pm 0.9_8$, $N = 311$). (C) Schematic of the proposed mechanism for thioctic acid packing with the slow addition of NaCl. (D) Extinction spectra of Au@TA nanoparticles equilibrated for 0−72 h. The inset shows an enlarged view of the extinction maxima (λ_{max} = 518 nm and ~521 nm for 0 and 16−72 h, respectively) in 20 mM sodium borate buffer (pH = 9).

functionalization. After exchange with thioctic acid, the λ_{max} shifts to ~521 nm. This value does not change significantly with increased incubation time and is indicative of stable, electromagnetically isolated nanostructures. Because thioctic acid chemisorbs to the surface of gold nanoparticles, the observed optical properties are consistent with an increase in local refractive index upon thioctic acid conjugation.

Surface Charge Characterization of Au@TA Nanoparticles. To verify that salt concentration is influencing the surface coverage of thioctic acid on the Au nanoparticle surfaces, zeta potential measurements (in mV) were carried out as a function of time in both the presence and absence of salt. Figure 2 summarizes these average (effective) surface charge data. For clarity, both control (no NaCl) and salt (with NaCl) data are plotted *versus* time (*i.e.*, the incubation time for gold nanoparticles in the thioctic acid solutions). It should be noted that the surface pK_a values for carboxylic acid terminated SAMs differ from solution values ranging from 4.5 to 7.[63−66] For all Au@TA nanoparticle samples studied, the surface potentials exhibit a negative value at pH = 9, which arise from the deprotonation of terminal

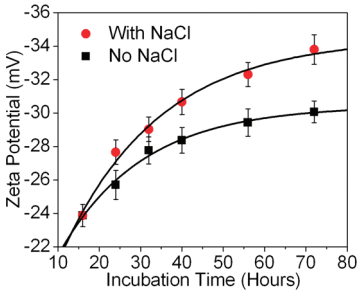

Figure 2. Zeta potential measurements for 2 nM Au@TA nanoparticles prepared in the presence and absence of NaCl. Nanoparticles were rinsed and suspended in 20 mM sodium borate buffer (pH = 9) prior to each measurement. The solid lines represent exponential fits for the zeta potential *vs* incubation time data: "No NaCl" $y = -14.7_5e^{-x/20.0} - 30.4_3$ and "With NaCl" $y = -20.5_2e^{-x/23.5} - 34.5_0$.

carboxyl acid groups of thioctic acid molecules bound to the nanostructures.

Previous studies revealed that carboxylic acid functionalized gold nanoparticles exhibited negative zeta potential values that ranged from 36 to 60 mV (pH 9).[63,67,68] As shown in Figure 2, the zeta potentials of Au@TA nanoparticles are dependent on both time and salt addition. In the absence of NaCl, the zeta potential magnitude ranges from −23.9 to −30.1 mV, a change of 6.2 mV, as incubation time increases. Similar trends are observed for Au@TA nanoparticles prepared in the presence of NaCl; however, the surface potentials range from −23.9 to −33.8 mV, a change of 9.9 mV, a change that is 60% greater than when salt is not present during ligand exchange.

To further investigate the differences between ligand exchange reactions in the absence and presence of salt, the zeta potential curves are evaluated using an exponential fit. From these fits, a (theoretical) saturated zeta potential is calculated at −30.4 and −34.5 mV for Au@TA nanoparticles incubated in the absence and presence of NaCl, respectively. Although the zeta potential magnitude increases with increasing incubation time, the addition of NaCl during thioctic acid functionalization produces a greater zeta potential magnitude increase (*vs* controls). These surface charge differences support that molecular surface coverage (*i.e.*, thioctic acid packing density) increases on gold nanoparticles when salt is present during functionalization *versus* control studies.

^{1}H NMR of Au@TA Nanoparticles. Recently, ^{13}C and ^{1}H NMR were applied to characterize molecules adsorbed to the surface of nanomaterials.[69] Four significant spectral characteristics are generally observed: (1) peak broadening,[70] (2) free ligand signatures superimposed on the surface-bound ligand spectrum,[71] (3) chemical shift differences between free ligand and surface-bound ligands,[71] and (4) magnetic field variations for the ligand that depend on the distance of the proton from the nanomaterial surface,[72] as well as on nanoparticle composition and size.[73,74] Similar observations are made for Au@TA nanoparticles. 2D COSY studies (Figure S2) were performed to determine the proton assignments shown in Figure 1A. In comparison to free ligand studies, spectral features for thioctic acid are significantly broadened when bound to gold nanoparticles (Figure S3), thereby verifying the molecules sampled are chemisorbed to the nanoparticle surface and not free in solution. This is an important spectral observation given that no superimposed bands are observed in these spectra.

TABLE 1. ^{1}H NMR Chemical Shifts, δ in ppm, for Thioctic Acid Free in Solution and Bound to Au Nanoparticles

proton assignment	free ligand (ppm)	nanoparticle bound (ppm)	chemical shift difference (δ ppm)
7	2.05	2.05	0.00
6	1.50	1.45	0.05
5	1.38	0.80	0.58
4	1.60, 1.70	1.10	0.50, 0.60
3	3.65	not observed	
2	1.90, 2.40	1.70, 2.10	0.20, 0.30
1	3.15	not observed	

Table 1 summarizes the average chemical shift data for thioctic acid free in solution (no nanoparticles) and bound to nanoparticle surfaces. At least four spectral features are notable. First, the methylene protons on carbons 7 and 6 exhibit no significant chemical shift differences between free and surface-bound ligands. This suggests that these protons are farthest from the nanoparticle surface and thereby possess the highest degree of entropy or solution-like behavior relative to the other protons.[75,76] Second, a greater degree of upfield chemical shift difference is observed for the methylene protons on carbons 5 and 4. As discussed previously, chemical shift differences between free and nanoparticle-bound NMR signatures increase as the distance from the nanoparticle surface decreases.[72] Following this reasoning, the degree of upfield shift differences for a given proton can be used to gauge its average distance from the nanoparticle surface relative to other protons. Finally, although the protons on carbon 2 are detectable, the protons on carbons 3 and 1 are not observed because of significant signal broadening, which leads to minimization of the signal-to-noise ratio of these peaks. As expected, these data suggest thioctic acid is attached to the surface of the gold nanoparticle via the dithiol ring with the carboxylic acid extending out into solution.

X-ray Photoelectron Spectroscopy of Au@TA Nanoparticles. Both LSPR and zeta potential data indicate that the slow addition of salt increases the packing density of thioctic acid on the gold nanoparticle surface. To verify this, quantitative information regarding the efficiency of thiol immobilization and the nature of thiol−gold interactions are probed using X-ray photoelectron

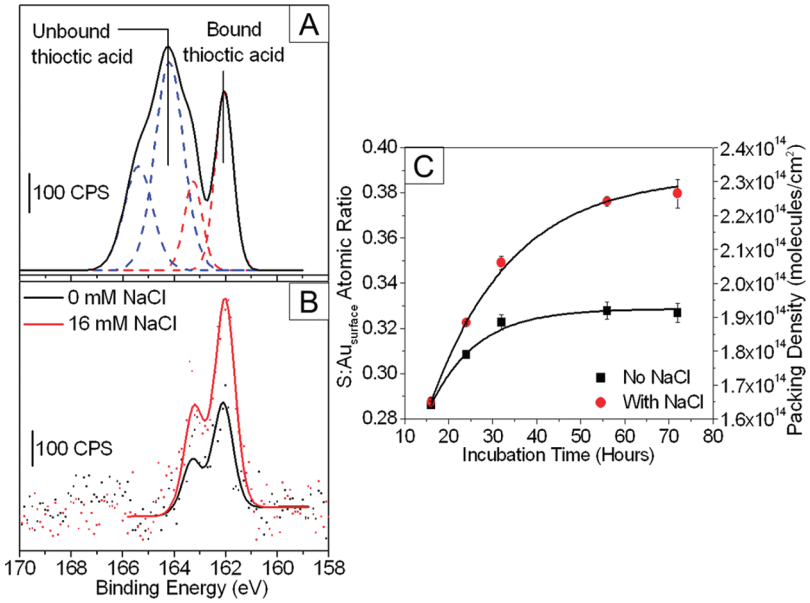

Figure 3. XPS characterization of Au@TA nanoparticles. (A) Normalized XPS spectra (S 2p) of Au@TA nanoparticles after one rinsing cycle. A S 2p doublet is observed for thioctic acid (doublet BE = 162.0 and 163.2 eV). (B) Normalized XPS spectra of Au@TA nanoparticles prepared in 0 and 16 mM NaCl (equilibration time =72 h) where the solid lines and dots correspond to the fitted and raw data, respectively. (C) Comparison of the S:$Au_{surface}$ atomic ratio (right-hand *y*-axis) and packing density (left-hand *y*-axis) *vs* incubation time for Au@TA nanoparticles prepared in the presence and absence of NaCl. The solid lines represent exponential fits for the S:$Au_{surface}$ atomic ratio *vs* incubation time: "No NaCl" $y = -0.19_8e^{-x/10.4} + 0.32_9$ and "With NaCl" $y = -0.24_0e^{-x/18.4} + 0.38_8$.

spectroscopy. Previously, thioctic acid functionalized gold thin film analysis revealed that the S 2p region exhibited a doublet with a 1.2 eV splitting energy and binding energies centered at ~162 and 163.2 eV for molecules directly bound to the gold surface.[77−82] As shown in Figure 3A, Au@TA nanoparticles that are rinsed once exhibit S 2p photoelectron spectral features consistent with bound and unbound thioctic acid molecules. Repeated rinsing, however, leads to the disappearance of the high binding energy (BE) S 2p bands associated with unbound thioctic acid.[83] Figure 3B reveals XPS spectra of Au@TA nanoparticles prepared in the absence and presence of salt after sufficient rinsing. In these data, a single S 2p doublet is observed. While the S 2p photoelectron spectra exhibit weak signal strengths because of the submonolayer to monolayer thioctic acid surface coverage on the nanoparticle surfaces, these findings indicate that the majority of the signal is attributed to surface-bound thioctic acid molecules.

To evaluate how incubation time and/or salt concentration impacts thioctic acid surface coverage, the S 2p doublet signal strength was monitored. Figure 3B compares S 2p spectra for Au@TA nanoparticles prepared after the addition of 0 and 16 mM NaCl upon incubation for 72 h. Signal correction of the S 2p peak area to the gold 4f peak area removed any interference caused by evaluating slightly different nanoparticle concentrations and samples. These data reveal that the addition of NaCl during thioctic acid functionalization increases the normalized S 2p peak area *versus*

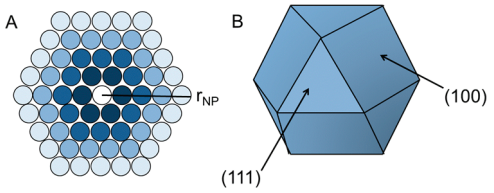

Figure 4. Schematic representation of a (A) gold nanoparticle cross section, which reveals concentric shells of gold atoms surrounding a central atom, and (B) Au atom Miller indices on the nanoparticle surface.

conditions when no salt is added. Moreover, the C 1s peak area and the O 1s peak area did not show any trends as a result of organic species contamination as the samples were prepared in ambient conditions (Figure S4).[84]

To quantitate the XPS data, the S 2p and Au 4f peak areas were converted to a S:Au atomic ratio using the empirical atomic sensitivity factor (SF) for each element (SF = 0.54 and 4.95 for S 2p and Au 4f, respectively).[85] Furthermore, because XPS interrogates a fraction of the total atomic layers, the Au XPS area must be corrected for the electron escape depth as follows:

$$\text{escape depth} = \lambda \cos(\theta) \quad (1)$$

where λ is the inelastic mean free path (IMFP) and θ is the angle between the surface normal and the direction of the emitted electron.[84,85] For these experiments θ is 0 and λ is $1.78 \pm 0.00_2$ nm where the IMFP is determined using the NIST Electron Inelastic Mean Free Path Database and the average kinetic energy of the Au 4f peaks.[86−88]

To apply this to a nanoparticle, the shell method must first be used to calculate the total number of atomic layers in a nanoparticle.[22,89] The shell method models a nanoparticle as a central atom that is surrounded by n shells (*i.e.*, layers) of gold atoms where the number of gold atoms in the nth shell can be calculated using the equation $10n^2 + 2$.[22,89] Next, the total number of shells per nanoparticle is calculated by dividing the nanoparticle radius ($r = d_{NP}/2$) by the gold atom diameter ($d_{Au} = 2.882$ Å) (Figure 4A). Dividing the escape depth by the diameter of a gold atom will yield the number of atomic layers signaled (N_{layer}) as follows:

$$N_{layer} = \frac{\lambda}{r_{Au}} = 6._2 \text{ layers} \quad (2)$$

where the number of layers is rounded to the closest whole number of shells in subsequent calculations.

Using these equations, a gold nanoparticle (d = 11.6 nm) contains 20 total shells but ~6 are sampled in these XPS conditions. The shell method can be applied to correct the S to Au atomic ratio ($S/Au_{surface}$) using the following equation:

$$\frac{S}{Au_{surface}} = \left[\frac{\sum_{n=15}^{20}(10n^2+2)}{10n^2+2}\right]\left[\frac{S}{Au}\right] \quad (3)$$

where the numerator in the first set of brackets is the number of total gold atoms signaled (n = 15 to 20) and the denominator is the number of surface gold atoms (n = 20). In the second set of brackets, S/Au represents the (sensitivity factor) corrected XPS signal.

In order to distinguish if increased thioctic acid SAM packing density arises from the systematic addition of NaCl or from increased incubation time with thioctic acid, the $S/Au_{surface}$ atomic ratio for gold nanoparticles incubated with thioctic acid in the absence and presence of NaCl are compared (Figure 3C). In both ligand exchange environments, the $S/Au_{surface}$ atomic ratio increases systematically with increasing thioctic acid incubation times. Figure 3C clearly displays that the $S/Au_{surface}$ atomic ratio saturates after an incubation period of 72 h. Additionally, while longer incubation times increase the number of thioctic acid molecules on the Au nanoparticle surfaces, salt mediates this process.[22,84−89] By applying an exponential fit to these data, a saturated $S/Au_{surface}$ atomic ratio of 0.32_9 and 0.38_8 is calculated for Au@TA nanoparticles incubated in the absence and presence of NaCl, respectively. In the absence of NaCl, these values imply that at least three gold atoms interact with one sulfur atom. In comparison, this value decreases to ~2.5 gold atoms interacting with each sulfur atom for SAMs prepared in the presence of NaCl. While the difference between the $S/Au_{surface}$ atomic ratio is small, a significant difference in the number of molecules on nanoparticle surfaces is indicated.

Expanding on these data, the packing density of thioctic acid SAMs on gold nanoparticle surfaces can be estimated. It should be noted that (1) the core size of Au@TA nanoparticles incubated in the absence and presence of NaCl do not change (Figure S1) and (2) the surface of ~12 nm gold nanoparticles contain predominately (100) surface planes (Figure 4B).[90,91] As a result, the packing density of atoms on the surface on the nanoparticle (σ_{hkl}) can be calculated as follows:

$$\sigma_{hkl} = \frac{4}{Qa^2(h^2+k^2+l^2)^{1/2}} \quad (4)$$

where Q is 2 for (100), and a is the bulk lattice parameter.

Next, the packing density of thioctic acid on Au@TA nanoparticle surfaces prepared in the absence and presence of salt can be approximated from XPS data as follows:

$$\text{packing density} = \left[\frac{S}{Au_{surface}}\right]\left[\frac{TA}{S}\right][\sigma_{100}] \quad (5)$$

where the corrected XPS signal (eq 3), the thioctic acid to sulfur ratio (2 sulfur atoms per thioctic molecule), and the gold atom packing density for a (100) surface plane are found in the first, second, and third brackets, respectively. For Au@TA nanoparticles prepared in the absence of salt, surface coverage is ~1.72×10^{14} molecules/cm^2 after 16 h of equilibration time and increases to 1.97×10^{14} molecules/cm^2 after equilibrating for 72 h. With systematic NaCl additions, Au@TA nanoparticles equilibrated for 16 h exhibit thioctic acid packing densities of 1.73×10^{14} molecules/cm^2 and increases to 2.29×10^{14} molecules/cm^2 after equilibrating for 72 h. The packing density calculations demonstrate that the slow addition of salt increases thioctic acid SAM packing density by 17% relative to the absence of salt after a 72 h incubation period. These values agree well with previously reported thioctic acid packing densities on flat gold surfaces, which range from 1.8×10^{14} to 2.1×10^{14} molecules/cm^2,[64,92−99] indicating XPS is an excellent technique to calculate SAM packing density on gold nanoparticles.

Electrostatic Interaction Energy and TA Self-Assembly. The LSPR, XPS, and zeta potential measurements suggest that the slow addition of salt increases the chemisorption of thioctic acid on gold nanoparticle surfaces, thereby resulting in an overall larger SAM surface coverage than when NaCl is omitted during ligand exchange reactions. We hypothesize that the mechanism of this effect is attributed to electrostatic interaction energy[100] differences (*i.e.*, decreased energy) between adjacent carboxylic acid terminal groups in the SAM as salt concentration increases. To model this, bulk ionic strength is used to estimate relative permittivity (ε_s) as follows:[101,102]

$$\varepsilon_s = 78.45 - \delta_s C_s + bC_s^{1.5} \quad (6)$$

where δ_S is the permittivity decrement (15.8 $L \cdot mol^{-1}$ when NaCl is the electrolyte), C_S is the electrolyte concentration, and b is a constant with a value of 3.01 $L^{2/3} \cdot mol^{-3/2}$. Next, Bjerrum lengths[103] are calculated as follows: $l_b = e^2/(4\pi\varepsilon_s\varepsilon_r k_b T)$ where e is the elementary charge, ε_r is permittivity of free space, k_b is the Boltzmann constant, and T is the temperature (294.3 K)). Additionally, inverse Debye lengths are calculated as follows: $\kappa = (8\pi l_b I)^{1/2}$. Subsequently, Debye lengths (κ^{-1})[103] are then calculated (Table 2) as a function of ionic strength (I). Finally, the electrostatic interfacial energy (E_{ij}^{EL} between two charged (carboxylic acid) molecules (i and j) is computed as follows:[100]

$$E_{ij}^{EL} = \frac{Z_i Z_j e^2}{4\pi\varepsilon_s\varepsilon_r} \frac{e^{-\kappa(l_b - \sigma)}}{(1+\kappa\sigma)l_b} \quad (7)$$

where Z_i and Z_j are the charge numbers for two deprotonated carboxylic acid groups, and σ is the Leonard-Jones potential for the carboxyl groups (0.305 nm).[104]

As shown in Figure 5A, increasing the ionic strength of the solution increases inverse Debye lengths and subsequently decreases the normalized electrostatic interfacial energy ($E_{ij}^{EL}/E_{ij,0}^{EL}$) between two adjacent molecules. This result is expected[100] as the effective spacing between two molecules (*i.e.*, l_b) and the effective Debye length of a charged molecule(s) should increase and decrease, respectively as ionic strength increases. This model supports the hypothesis that the electrostatic interfacial energy between two molecules decreases as salt concentration increases.

To investigate how the electrostatic interfacial energy impacts SAM formation and packing density saturation on gold nanoparticles in the presence and absence of salt, the average spacing between TA molecules was estimated using XPS packing densities and Spartan. Importantly, the dimension of the carboxylic acid terminal group is estimated using the length between the oxygen atoms (2.23 Å) and the covalent radius of an oxygen atom (0.63 Å). Assuming a rectangular molecular footprint for the carboxylic acid group, the average spacing between TA molecules is calculated. Finally, the electrostatic interfacial energy is determined using eq 7, where l_b is the average distance between two SAM ligands.

As shown in Figure 5B, the electrostatic interfacial energy between SAM ligands increases with packing density when formed both in the presence and in the absence of salt. Dashed lines indicate saturated packing densities in the absence and presence of salt. Notably, this energy increases more rapidly and saturates at a lower packing density when the SAM forms in the absence of salt (ionic strength = $1._3$ mM) *versus* the presence of salt. In the presence of salt, the normalized electrostatic interfacial energy between surface-bound ligands decreases by ~4% *versus* the low ionic strength time control studies. We attribute this difference to shorter Debye lengths in the relatively higher ionic strength ligand exchange conditions. Importantly, these interfacial energetic differences would facilitate the accessibility of pinhole defects in the SAM layer,[105] allowing these sites to be more easily filled by additional thioctic acid molecules.

TABLE 2. Calculated Debye Lengths as a Function of NaCl Concentration and Ionic Strength

[NaCl] (mM)	I (mM)	κ^{-1} (nm)
0	1.2_6	8.5_1
3.6_3	4.8_8	4.3_2
7.2_5	8.5_0	3.2_7
14.4_4	15.6_9	2.4_1

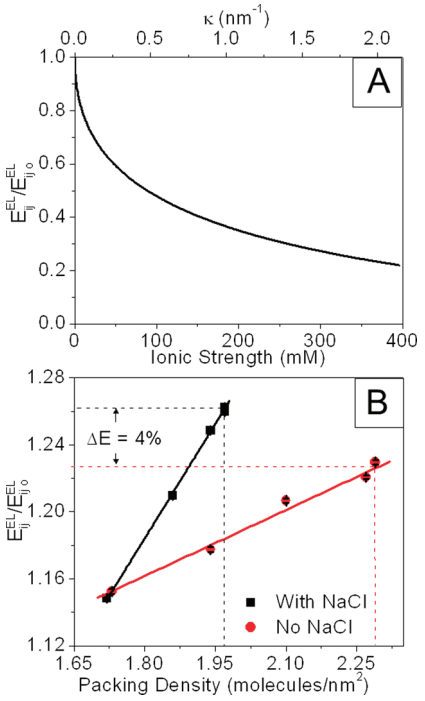

Figure 5. Calculated electrostatic interfacial energies between two terminal carboxylic acid groups. (A) Normalized electrostatic interfacial energy as a function of ionic strength (lower *x*-axis) and inverse Debye length (upper *x*-axis). (B) Normalized electrostatic interfacial energy as a function of thioctic acid packing density for exchange reactions that occurred in the absence and presence of salt. Dashed lines indicate the estimated packing density saturation values and corresponding normalized electrostatic interfacial energies. Error bars are contained within the size of the data points and represent propagated error.

Evaluation of Au@TA Nanoparticle Stability. To further investigate how SAM packing density impacts nanostructure stability, the flocculation parameter[80,106,107] for Au@TA nanoparticles incubated for 72 h in the absence and presence of NaCl was evaluated. Flocculation parameter studies can be used to gain

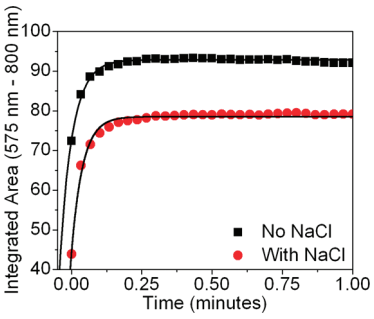

Figure 6. Normalized integrated area for Au@TA nanoparticles incubated for 72 h in the presence and absence of salt. Extinction spectra of Au@TA nanoparticles in buffer (pH = 5.5) were integrated at λ = 575−800 nm to semiquantify flocculation.

semiquantitative information about the nanostructure stability by monitoring changes in extinction as a function of solution pH and/or time.[80,106,107] As nanoparticle flocculation increases, the extinction intensity at ~521 nm decreases while a new lower energy band at 650 nm intensifies (Figure S5). Next, the extinction spectra were integrated from 575−800 nm to quantify the degree of nanoparticle flocculation as a function of time (Figure 6). In pH 5.5 buffer, the integrated area increases as a function of time and at different rates for the two nanoparticle samples. To compare the stability of the Au@TA nanoparticles, the integrated data were used to determine when flocculation reached its maximum. Larger values are indicative of more stable nanostructures.[107] The Au@TA nanoparticles incubated without NaCl flocculated within 26 s, whereas the Au@TA nanoparticles incubated in the presence of NaCl flocculated in twice the time. Significantly, these flocculation studies reveal that salt-mediated thioctic acid self-assembly increases the stability of the Au@TA nanoparticles by ~20% *versus* controls.

CONCLUSIONS

In summary, gold nanoparticles functionalized with thioctic acid were prepared with the slow addition of NaCl. TEM, ^{1}H NMR, extinction spectroscopy, zeta potential, XPS, and flocculation studies determined that the self-assembly of thioctic acid on gold nanoparticles increases with increasing NaCl concentration. Quantitative information regarding the fraction of pinhole and collapsed defect sites on gold nanoparticles was not evaluated; however, salt facilitated the self-assembly process. First, an increase in NaCl decreases the Debye length of the deprotonated carboxylate groups on the assembled thioctic acid molecules thereby (1) reducing the electrostatic interfacial energy between adjacent molecules and (2) facilitating increased SAM packing densities. Furthermore, the slow addition of NaCl to gold nanoparticles during thioctic acid self-assembly increased subsequent functionalized nanoparticle stability *versus* controls as determined from flocculation studies. We expect these results to improve strategies for reproducible SAM formation on solution-phase nanostructures. Future studies could be expanded to investigate how nanoparticle shape, size, and radius of curvature impact this self-assembly process for ultimate improvements in the reproducible synthesis and use of nanomaterials in a variety of applications.

METHODS

Materials. Gold(III) chloride trihydrate ($HAuCl_4$), trisodium citrate dihydrate (citrate), thioctic acid, boric acid, and sodium tetraborate decahydrate were purchased from Sigma Aldrich (St. Louis, MO). Sodium chloride (NaCl), sodium hydroxide (NaOH), ethanol, hydrochloric acid (HCl), and nitric acid (HNO_3) were purchased from Fisher Scientific (Pittsburgh, PA). Nanopure water (18.2 MΩ cm^{-1}) was obtained from a Barnstead Nanopure System and used for all experiments.

Preparation of Citrate-Stabilized Au (Au@citrate) Nanoparticles. All glassware used in the preparation and storage of Au nanoparticles was cleaned with aqua regia (3:1 HCl/HNO_3), rinsed with water, and oven-dried. Gold nanoparticles were prepared according to previous reports.[108] Briefly, a 200 mL aqueous solution of 1 mM $HAuCl_4$ was refluxed while stirring vigorously. Next, 20 mL of 38.8 mM citrate was quickly added, refluxed for 10 min, and allowed to cool to room temperature while stirring. The resulting gold nanoparticles had a diameter of $11.6_9 \pm 0.9_8$ nm as determined by TEM and an extinction maximum, λ_{max} = 518 nm.

Preparation of Au@TA Nanoparticles. Au@TA nanoparticles were prepared by modifying a previously published method.[63] First, Au@citrate nanoparticles were filtered (0.45 μm filter) (Whatman, Middlesex, UK) and centrifuged (Eppendorf, model 5424 centrifuge, Germany; 11 500 rpm (8797*g*) for 40 min) to remove large aggregates and excess citrate, respectively. The resulting pellet was suspended in pH-adjusted water (pH = 11 with 1 M NaOH) to a nanoparticle concentration of 10 nM according to the method described by Haiss.[109] Thioctic acid functionalization was carried out by adding 10 mM thioctic acid (1000 μL in ethanol) to 10 mL aliquots of 10 nM Au@citrate nanoparticles. This solution was allowed to stir in the dark for at least 16 h at 20 °C.

During the slow addition of salt,[110] a 2 M NaCl solution was added dropwise to Au@TA nanoparticles until the salt concentration of salt reached 3.6 mM. This solution was allowed to stir (slowly) for 8 h. The NaCl concentration was then increased to 7.2 and 14.4 mM in similar subsequent steps. After each of these incubation periods, excess thioctic acid and NaCl were removed by centrifugation at 11 500 rpm (8797*g*) for 40 min. In order to investigate the effect of time on the samples incubated in the presence of 16 mM NaCl, the samples were allowed to equilibrate for an additional 32 h. Prior to measurements, these samples were centrifuged at 11 500 rpm (8797*g*) for 40 min. Following removal of the supernatant, the nanoparticle pellet was resuspended in pH-adjusted water (pH = 11). This rinsing process was repeated three times. Samples in which no salt was added but allowed to incubate in thioctic acid solutions were used as a control.

TEM. The homogeneity and diameter of the nanoparticles were characterized using TEM (JEOL JEM-1230). Samples were prepared by applying 30 μL of a diluted nanoparticle solution (50% mixture in ethanol) to a carbon Formvar coated copper grid (400 mesh, Electron Microscopy Sciences, Hatfield, PA). Excess solution

was removed with filter paper, and the sample was allowed to dry. The resulting images were analyzed using Image Pro Analyzer, and at least 100 nanoparticles were evaluated per sample.

NMR Spectroscopy. ^{1}H NMR and 2D COSY spectra were recorded on a Bruker 600 mHz spectrometer (Bruker Biospin Corp., Billerica, MA). Samples were prepared by centrifugation at 15 000 rpm (14967*g*) for 30 min. After the supernatant was removed, the nanoparticles were resuspended in pH-adjusted water (pH = 11) (repeated three times). Next, the samples were transferred to a lyophilizing vessel, flash frozen with liquid N_2, lyophilized to remove water, and resuspended in D_2O to a 50 nM nanoparticle concentration. Spectra were analyzed using Topspin and Nuts. Chemical shifts were referenced to the residual shifts of the deuterated solvent. 2D COSY spectra were acquired using standard pulse sequences optimized to the individual parameters of each sample. These data were used for proton assignments in the 1D spectra.

Extinction Spectroscopy. Extinction spectra of Au@TA nanoparticles were acquired using a UV−visible spectrometer (Ocean Optics HR 4000) configured in transmission geometry. Before acquiring spectra, samples were centrifuged at 11 500 rpm (8797*g*) for 40 min and redispersed in 20 mM sodium borate buffer (pH = 9). The solution was diluted to a final nanoparticle concentration of 2 nM using the same buffer. All spectra were collected in disposable methacrylate cuvettes (path length = 0.5 cm) using the following parameters: integration time = 20 ms, average = 20 scans, and boxcar = 10.

Zeta Potential. Effective gold nanoparticle surface charges (zeta potential) were determined from their electrophoretic mobility at 25 °C using a Malvern Zetasizer (Worcestershire, UK). Au@TA nanoparticle samples were centrifuged at 11 500 rpm (8797*g*) for 40 min, redispersed in 20 mM sodium borate buffer (pH = 9), and diluted to a final concentration of 2 nM. Monomodal acquisitions and fits according to the Smoluchowski theory were used. Measurements were performed in triplicate, and error bars represent the standard deviation of these data.

XPS. XPS measurements were collected using a Kratos Axis Ultra spectrometer with a monochromatic Al Kα X-ray source as described previously.[111] Briefly, a 160 eV pass energy, 1 eV step size, 200 ms dwell time, and ∼700 μm × 300 μm X-ray spot size were used for a survey scan (range = 1200 to −5 eV). Region scans (O 1s, C 1s, S 2p, and Au 4f) exhibited typical band widths of 20−50 eV, 20 eV pass energies, 0.1 eV step sizes, and 1 s dwell times. All spectra were analyzed using CasaXPS and were charge-calibrated with respect to the adventitious C 1s peak at 285.0 eV. The S 2p peak of thioctic acid was peak fitted using the S 2p doublet with a 2:1 area ratio and an energy difference of 1.2 eV. A Shirley background was used to subtract the inelastic background from the S 2p and Au 4f signal. The curves were fit using a Gaussian/Lorentzian (GL(30)) line shape. To account for differences in nanoparticle concentration in sample spots, the S 2p areas were normalized using the Au 4f area. Two areas were analyzed per sample. Error bars represent the standard deviation of these data.

Flocculation Parameter. Au@TA nanoparticle solutions (10 nM) were prepared in pH 11 water. To monitor flocculation, gold nanoparticles were incubated for 72 h in the absence and presence of salt, centrifuged, and redispersed to 3.0 mS cm^{-1} sodium acetate and phosphate buffer (pH 5.5 and 12, respectively). The solution was stirred, and extinction spectra were collected every 2 s. The data were baseline subtracted using an in-house written MatLab program. Briefly, LSPR spectra collected in pH 12 buffer were aligned to 0 AU at 800 nm and subsequently used to determine a normalization factor that was applied to all other spectra. Integrated areas were calculated from these normalized spectra (from 575 to 800 nm) collected in pH 5.5 buffer and plotted as a function of time.

Acknowledgment. The authors gratefully acknowledge financial support from the Roy J. Carver Charitable Trust and NIH-NCRR 1UL1RR024979, 1KL2RR024980, and 1TL1RR024981, University of Iowa Clinical and Translational Science Program. Any opinions, findings, and conclusions or recommendations expressed in this material are those of the authors and do not necessarily reflect the views of the National Institutes of Health. S. Valupillai is acknowledged for assistance with NMR.

Supporting Information Available: Transmission electron microscopy, ^{1}H NMR and 2D COSY spectra with peak assignments for Au@TA nanoparticles, XPS spectral C 1s and O 1s region scans for C region scans, and extinction spectra for flocculation parameter studies are provided. This material is available free of charge *via* the Internet at http://pubs.acs.org.

REFERENCES AND NOTES

1. Ulman, A. Formation and Structure of Self-assembled Monolayers. *Chem. Rev.* **1996**, *96*, 1533–1554.
2. Hickman, J. J.; Ofer, D.; Laibinis, P. E.; Whitesides, G. M.; Wrighton, M. S. Molecular Self-Assembly of 2-Terminal, Voltammetric Microsensors with Internal References. *Science* **1991**, *252*, 688–691.
3. Mirkin, C. A.; Ratner, M. A. Molecular Electronics. *Annu. Rev. Phys. Chem.* **1992**, *43*, 719–754.
4. Wollman, E. W.; Kang, D.; Frisbie, C. D.; Lorkovic, I. M.; Wrighton, M. S. Photosensitive Self-Assembled Monolayers on Gold−Photochemistry of Surface-Confined Aryl Azide and Cyclopentadienylmanganese Tricarbonyl. *J. Am. Chem. Soc.* **1994**, *116*, 4395–4404.
5. Bonnemann, H.; Richards, R. M. Nanoscopic Metal Particles−Synthetic Methods and Potential Applications. *Eur. J. Inorg. Chem.* **2001**, 2455–2480.
6. Noh, J.; Kato, H. S.; Kawai, M.; Hara, M. Surface Structure and Interface Dynamics of Alkanethiol Self-assembled Monolayers on Au(111). *J. Phys. Chem. B* **2006**, *110*, 2793–2797.
7. Dameron, A. A.; Charles, L. F.; Weiss, P. S. Structures and Displacement of 1-Adamantanethiol Self-Assembled Monolayers on Au(111). *J. Am. Chem. Soc.* **2005**, *127*, 8697–8704.
8. Crooks, R. M.; Ricco, A. J. New Organic Materials Suitable for Use in Chemical Sensor Arrays. *Acc. Chem. Res.* **1998**, *31*, 219–227.
9. Badia, A.; Lennox, R. B.; Reven, L. A Dynamic View of Self-assembled Monolayers. *Acc. Chem. Res.* **2000**, *33*, 475–481.
10. Adams, D. M.; Brus, L.; Chidsey, C. E. D.; Creager, S.; Creutz, C.; Kagan, C. R.; Kamat, P. V.; Lieberman, M.; Lindsay, S.; Marcus, R. A.; *et al.* Charge Transfer on the Nanoscale: Current Status. *J. Phys. Chem. B* **2003**, *107*, 6668–6697.
11. Fendler, J. H. Chemical Self-assembly for Electronic Applications. *Chem. Mater.* **2001**, *13*, 3196–3210.
12. Si, S.; Mandal, T. K. pH-Controlled Reversible Assembly of Peptide-Functionalized Gold Nanoparticles. *Langmuir* **2006**, *23*, 190–195.
13. Brust, M.; Walker, M.; Bethell, D.; Schiffrin, D. J.; Whyman, R. Synthesis of Thiol-Derivatized Gold Nanoparticles in a 2-Phase Liquid-Liquid System. *J. Chem. Soc., Chem. Commun.* **1994**, 801–802.
14. Weare, W. W.; Reed, S. M.; Warner, M. G.; Hutchison, J. E. Improved Synthesis of Small (d_{CORE} ∼ 1.5 nm) Phosphine-Stabilized Gold Nanoparticles. *J. Am. Chem. Soc.* **2000**, *122*, 12890–12891.
15. Joo, S. W.; Kim, W. J.; Yoon, W. S.; Choi, I. S. Adsorption of 4,4'-Biphenyl Diisocyanide on Gold Nanoparticle Surfaces Investigated by Surface-enhanced Raman Scattering. *J. Raman Spectrosc.* **2003**, *34*, 271–275.
16. Yang, A.-C.; Weng, C.-I. Structural and Dynamic Properties of Water near Monolayer-Protected Gold Clusters with Various Alkanethiol Tail Groups. *J. Phys. Chem. C* **2010**, *114*, 8697–8709.
17. Creager, S. E.; Clarke, J. Contact-Angle Titrations of Mixed-Mercaptoalkanoic Acid/Alkanethiol Monolayers on Gold. Reactive *vs.* Nonreactive Spreading, and Chain Length Effects of Surface pK_a Values. *Langmuir* **1994**, *10*, 3675–3683.
18. Tseng, W.-L.; Huang, M.-F.; Huang, Y.-F.; Chang, H.-T. Nanoparticle-Filled Capillary Electrophoresis for the Separation of Long DNA Molecules in the Presence of Hydrodynamic and Electrokinetic Forces. *Electrophoresis* **2005**, *26*, 3069–3075.
19. Haes, A. J.; Hall, W. P.; Chang, L.; Klein, W. L.; Van Duyne, R. P. A Localized Surface Plasmon Resonance Biosensor: First Steps Toward an Assay for Alzheimer's Disease. *Nano Lett.* **2004**, *4*, 1029–1034.

20. Haes, A. J.; Zhao, J.; Zou, S.; Own, C. S.; Marks, L. D.; Schatz, G. C.; Van Duyne, R. P. Solution-Phase, Triangular Ag Nanotriangles Fabricated by Nanosphere Lithography. *J. Phys. Chem. B* **2005**, *109*, 11158–11162.
21. Templeton, A. C.; Wuelfing, M. P.; Murray, R. W. Monolayer Protected Cluster Molecules. *Acc. Chem. Res.* **2000**, *33*, 27–36.
22. Daniel, M. C.; Astruc, D. Gold Nanoparticles: Assembly, Supramolecular Chemistry, Quantum-size-related Properties, and Applications toward Biology, Catalysis, and Nanotechnology. *Chem. Rev.* **2004**, *104*, 293–346.
23. Chechik, V. Reduced Reactivity of Aged Au Nanoparticles in Ligand Exchange Reactions. *J. Am. Chem. Soc.* **2004**, *126*, 7780–7781.
24. Hill, H. D.; Millstone, J. E.; Banholzer, M. J.; Mirkin, C. A. The Role Radius of Curvature Plays in Thiolated Oligonucleotide Loading on Gold Nanoparticles. *ACS Nano* **2009**, *3*, 418–424.
25. Zhang, S.; Leem, G.; Lee, T. R. Monolayer-Protected Gold Nanoparticles Prepared Using Long-Chain Alkanethioacetates. *Langmuir* **2009**, *25*, 13855–13860.
26. Leontowich, A. F. G.; Calver, C. F.; Dasog, M.; Scott, R. W. J. Surface Properties of Water-Soluble Glycine-Cysteamine-Protected Gold Clusters. *Langmuir* **2010**, *26*, 1285–1290.
27. Sardar, R.; Heap, T. B.; Shumaker-Parry, J. S. Versatile Solid Phase Synthesis of Gold Nanoparticle Dimers Using an Asymmetric Functionalization Approach. *J. Am. Chem. Soc.* **2007**, *129*, 5356–5357.
28. Wang, G. L.; Murray, R. W. Controlled Assembly of Monolayer-protected Gold Clusters by Dissolved DNA. *Nano Lett.* **2004**, *4*, 95–101.
29. Warner, M. G.; Hutchison, J. E. Linear Assemblies of Nanoparticles Electrostatically Organized on DNA Scaffolds. *Nat. Mat.* **2003**, *2*, 272–277.
30. Wyrwa, D.; Beyer, N.; Schmid, G. One-dimensional Arrangements of Metal Nanoclusters. *Nano Lett.* **2002**, *2*, 419–421.
31. DeVries, G. A.; Brunnbauer, M.; Hu, Y.; Jackson, A. M.; Long, B.; Neltner, B. T.; Uzun, O.; Wunsch, B. H.; Stellacci, F. Divalent Metal Nanoparticles. *Science* **2007**, *315*, 358–361.
32. Sardar, R.; Shumaker-Parry, J. S. Asymmetrically Functionalized Gold Nanoparticles Organized in One-dimensional Chains. *Nano Lett.* **2008**, *8*, 731–736.
33. Phillips, R. L.; Miranda, O. R.; You, C. C.; Rotello, V. M.; Bunz, U. H. F. Rapid and Efficient Identification of Bacteria using Gold-nanoparticle–Poly(para-phenyleneethynylene) Constructs. *Angew. Chem.* **2008**, *47*, 2590–2594.
34. Thomas, K. G.; Kamat, P. V. Chromophore-functionalized Gold Nanoparticles. *Acc. Chem. Res.* **2003**, *36*, 888–898.
35. Marinakos, S. M.; Brousseau, L. C.; Jones, A.; Feldheim, D. L. Template Synthesis of One-dimensional Au, Au-poly(pyrrole), and Poly(pyrrole) Nanoparticle Arrays. *Chem. Mater.* **1998**, *10*, 1214–1219.
36. Shipway, A. N.; Lahav, M.; Blonder, R.; Willner, I. Bis-bipyridinium Cyclophane Receptor Au Nanoparticle Superstructures for Electrochemical Sensing Applications. *Chem. Mater.* **1999**, *11*, 13–15.
37. Katz, E.; Willner, I. Integrated Nanoparticle-biomolecule Hybrid Systems: Synthesis, Properties, and Applications. *Angew. Chem.* **2004**, *43*, 6042–6108.
38. Ghosh, P. S.; Kim, C. K.; Han, G.; Forbes, N. S.; Rotello, V. M. Efficient Gene Delivery Vectors by Tuning the Surface Charge Density of Amino Acid-functionalized Gold Nanoparticles. *ACS Nano* **2008**, *2*, 1335–1344.
39. Bastus, N. G.; Sanchez-Tillo, E.; Pujals, S.; Farrera, C.; Lopez, C.; Giralt, E.; Celada, A.; Lloberas, J.; Puntes, V. Homogeneous Conjugation of Peptides onto Gold Nanoparticles Enhances Macrophage Response. *ACS Nano* **2009**, *3*, 1335–1344.
40. Selvakannan, P.; Mandal, S.; Phadtare, S.; Pasricha, R.; Sastry, M. Capping of Gold Nanoparticles by the Amino Acid Lysine Renders Them Water-Dispersible. *Langmuir* **2003**, *19*, 3545–3549.
41. Heeb, R.; Lee, S.; Venkataraman, N.; Spencer, N. D. Influence of Salt on the Aqueous Lubricaiton Properties of End Grafted, Ethylene Glycol-Based Self-Assembled Monolayers. *Appl. Mater. Interfaces* **2009**, *1*, 1105–1112.
42. Finklea, H. O. Electrochemistry of Organized Monolayers of Thiols and Related Molecules on Electrodes. *Electroanal. Chem.: Ser. Adv.* **1996**, *19*, 109–335.
43. Preiner, M. J.; Melosh, N. A. Identification and Passivation of Defects in Self-Assembled Monolayers. *Langmuir* **2009**, *25*, 2585–2587.
44. Lusk, A. T.; Jennings, G. K. Characterization of Self-assembled Monolayers Formed from Sodium s-Alkyl Thiosulfates on Copper. *Langmuir* **2001**, *17*, 7830–7836.
45. Campuzano, S.; Pedrero, M.; Montemayor, C.; Fatas, E.; Pingarron, J. M. Characterization of Alkanethiol Self-assembled Monolayers-Modified Gold Electrodes by Electrochemical Impedance Spectroscopy. *J. Electroanal. Chem.* **2006**, *586*, 112–121.
46. Kwon, S.; Choi, J.; Lee, H.; Noh, J. Molecular-scale Investigation of Octanethiol Self-assembled Monolayers on Au(111) Prepared by Solution and Vapor Deposition at High Temperature. *Colloids Surf., A* **2008**, *313*, 324–327.
47. Yamada, R.; Wano, H.; Uosaki, K. Effect of Temperature on Structure of the Self-assembled Monolayer of Decanethiol on Au(111) Surface. *Langmuir* **2000**, *16*, 5523–5525.
48. Poirier, G. E. Mechanism of Formation of Au Vacancy Islands in Alkanethiol Monolayers on Au(111). *Langmuir* **1997**, *13*, 2019–2026.
49. Losic, D.; Shapter, J. G.; Gooding, J. J. Atomically Flat Gold for Biomolecule Immobilization and Imaging. *Aust. J. Chem.* **2001**, *54*, 643–648.
50. Losic, D.; Gooding, J. J.; Shapter, J. G.; Hibbert, D. B.; Short, K. The Influence of the Underlying Gold Substrate on Glucose Oxidase Electrodes Fabricated using Self-assembled Monolayers. *Electroanalysis* **2001**, *13*, 1385–1393.
51. Losic, D.; Shapter, J. G.; Gooding, J. J. Influence of Surface Topography on Alkanethiol SAMs Assembled from Solution and by Microcontact Printing. *Langmuir* **2001**, *17*, 3307–3316.
52. Kreibig, U. Optics of Nanosized Metals. In *Handbook of Optical Properties*; Hummel, R. E.; Wissmann, P., Eds.; CRC Press: Boca Raton, 1997; Vol. II, pp 145–190.
53. Haes, A. J.; Haynes, C. L.; McFarland, A. D.; Schatz, G. C.; Van Duyne, R. P.; Zou, S. Plasmonic Materials for Surface-enhanced Sensing and Spectroscopy. *MRS Bull.* **2005**, *30*, 368–375.
54. El-Sayed, M. A. Some Interesting Properties of Metals Confined in Time and Nanometer Space of Different Shapes. *Acc. Chem. Res.* **2001**, *34*, 257–264.
55. Link, S.; El-Sayed, M. A. Spectral Properties and Relaxation Dynamics of Surface Plasmon Electronic Oscillations in Gold and Silver Nano-dots and Nano-rods. *J. Phys. Chem. B* **1999**, *103*, 8410–8426.
56. Bohren, C. F.; Huffman, D. R. *Absorption and Scattering of Light by Small Particles*; Wiley Interscience: New York, 1983.
57. Schmid, G. Large Clusters and Colloids–Metals in the Embryonic State. *Chem. Rev.* **1992**, *92*, 1709–1727.
58. Aslan, K.; Perez-Luna, V. H. Surface Modification of Colloidal Gold by Chemisorption of Alkanethiols in the Presence of a Nonionic Surfactant. *Langmuir* **2002**, *18*, 6059–6065.
59. Pham, T.; Jackson, J. B.; Halas, N. J.; Lee, T. R. Preparation and Characterization of Gold Nanoshells Coated with Self-assembled Monolayers. *Langmuir* **2002**, *18*, 4915–4920.
60. Haynes, C. L.; Haes, A. J.; McFarland, A. D.; Van Duyne, R. P. Nanoparticles with Tunable Localized Surface Plasmon Resonances. In *Topics in Fluorescence*; Lakowicz, J. R., Ed.; Plenum Press: New York, 2003; Vol. 8, pp 1–54.
61. Haynes, C. L.; McFarland, A. D.; Van Duyne, R. P. Surface-enhanced Raman Spectroscopy. *Anal. Chem.* **2005**, *77*, 338A–346A.
62. Mie, G. Contributions to the Optics of Turbid Media, Especially Colloidal Metal Solutions. *Ann. Phys.* **1908**, *25*, 377–445.
63. Ivanov, M. R.; Bednar, H. R.; Haes, A. J. Investigations of the Mechanism of Gold Nanoparticle Stability and Surface Functionalization in Capillary Electrophoresis. *ACS Nano* **2009**, *3*, 386–394.

64. Rooth, M.; Shaw, A. M. pH-Controlled Formation Kinetics of Self-assembled Layers of Thioctic Acid on Gold Nanoparticles. *J. Phys. Chem. C* **2007**, *111*, 15363–15369.
65. Cheng, Q.; Brajter-Toth, A. Selectivity and Sensitivity of Self-Assembled Thioctic Acid Electrodes. *Anal. Chem.* **1992**, *64*, 1998–2000.
66. Cheng, Q.; BrajterToth, A. Permselectivity Sensitivity, and Amperometric pH Sensing at Thioctic Acid Monolayer Microelectrodes. *Anal. Chem.* **1996**, *68*, 4180–4185.
67. Kimura, K.; Takashima, S.; Ohshima, H. Molecular Approach to the Surface Potential Estimate of Thiolate-modified Gold Nanoparticles. *J. Phys. Chem. B* **2002**, *106*, 7260–7266.
68. Dougherty, G. M.; Rose, K. A.; Tok, J. B. H.; Pannu, S. S.; Chuang, F. Y. S.; Sha, M. Y.; Chakarova, G.; Penn, S. G. The Zeta Potential of Surface-functionalized Metallic Nanorod Particles in Aqueous Solution. *Electrophoresis* **2008**, *29*, 1131–1139.
69. Song, Y.; Harper, A. S.; Murray, R. W. Ligand Heterogeneity on Monolayer-Protected Gold Clusters. *Langmuir* **2005**, *21*, 5492–5500.
70. Hostetler, M. J.; Wingate, J. E.; Zhong, C.-J.; Harris, J. E.; Vachet, R. W.; Clark, M. R.; Londono, J. D.; Green, S. J.; Stokes, J. J.; Wignall, G. D.; *et al.* Alkanethiolate Gold Cluster Molecules with Core Diameters from 1.5 to 5.2 nm: Core and Monolayer Properties as a Function of Core Size. *Langmuir* **1998**, *14*, 17–30.
71. Badia, A.; Gao, W.; Singh, S.; Demers, L.; Cuccia, L.; Reven, L. Structure and Chain Dynamics of Alkanethiol-Capped Gold Colloids. *Langmuir* **1996**, *12*, 1262–1269.
72. Terrill, R. H.; Postlethwaite, T. A.; Chen, C.-h.; Poon, C.-D.; Terzis, A.; Chen, A.; Hutchison, J. E.; Clark, M. R.; Wignall, G. Monolayers in Three Dimensions: NMR, SAXS, Thermal, and Electron Hopping Studies of Alkanethiol Stabilized Gold Clusters. *J. Am. Chem. Soc.* **2002**, *117*, 12537–12548.
73. Crespo, P.; Litrán, R.; Rojas, T. C.; Multigner, M.; de la Fuente, J. M.; Sánchez-López, J. C.; García, M. A.; Hernando, A.; Penadés, S.; Fernández, A. Permanent Magnetism, Magnetic Anisotropy, and Hysteresis of Thiol-Capped Gold Nanoparticles. *Phys. Rev. Lett.* **2004**, *93*, 087204.
74. Hori, H.; Yamamato, T.; Iwamoto, T. Diameter Dependence of Ferromagnetic Spin Moment in Au Nanocrystals. *Phys. Rev. B* **2004**, *69*, 174411.
75. Kohlmann, O.; Steinmetz, W. E.; Mao, X.-A.; Wuelfing, W. P.; Templeton, A. C.; Murray, R. W.; Johnson, C. S. NMR Diffusion, Relaxation, and Spectroscopic Studies of Water Soluble, Monolayer-Protected Gold Nanoclusters. *J. Phys. Chem. B* **2001**, *105*, 8801–8809.
76. Schmitt, H.; Badia, A.; Dickinson, L.; Reven, L.; Lennox, R. B. The Effect of Terminal Hydrogen Bonding on the Structure and Dynamics of Nanoparticle Self-Assembled Monolayers (SAMs): An NMR Dynamics Study. *Adv. Mater.* **1998**, *10*, 475–480.
77. Park, J. N.; Forman, A. J.; Tang, W.; Cheng, J. H.; Hu, Y. S.; Lin, H. F.; McFarland, E. W. Highly Active and Sinter-Resistant Pd-Nanoparticle Catalysts Encapsulated in Silica. *Small* **2008**, *4*, 1694–1697.
78. Zhang, S. S.; Leem, G.; Srisombat, L. O.; Lee, T. R. Rationally Designed Ligands that Inhibit the Aggregation of Large Gold Nanoparticles in Solution. *J. Am. Chem. Soc.* **2008**, *130*, 113–120.
79. Porter, L. A.; Ji, D.; Westcott, S. L.; Graupe, M.; Czernuszewicz, R. S.; Halas, N. J.; Lee, T. R. Gold and Silver Nanoparticles Functionalized by the Adsorption of Dialkyl Disulfides. *Langmuir* **1998**, *14*, 7378–7386.
80. Weisbecker, C. S.; Merritt, M. V.; Whitesides, G. M. Molecular Self-Assembly of Aliphatic Thiols on Gold Colloids. *Langmuir* **1996**, *12*, 3763–3772.
81. Johnson, S. R.; Evans, S. D.; Mahon, S. W.; Ulman, A. Alkanethiol Molecules Containing an Aromatic Moiety Self-assembled onto Gold Clusters. *Langmuir* **1997**, *13*, 51–57.
82. Lu, H. B.; Campbell, C. T.; Castner, D. G. Attachment of Functionalized Poly(ethylene glycol) Films to Gold Surfaces. *Langmuir* **2000**, *16*, 1711–1718.
83. Castner, D. G.; Hinds, K.; Grainger, D. W. X-ray Photoelectron Spectroscopy Sulfur 2p Study of Organic Thiol and Disulfide Binding Interactions with Gold Surfaces. *Langmuir* **1996**, *12*, 5083–5086.
84. Baer, D. R.; Engelhard, M. H. XPS Analysis of Nanostructured Materials and Biological Surfaces. *J. Electron Spectrosc. Relat. Phenom.* **2010**, *178*, 415–432.
85. Lumsden, J. B. X-Ray Photoelectron Spectroscopy. In *Materials Characterization*; Whan, R. E., Ed.; American Society for Metals: Metals Park, OH, 1986; Vol. 10, pp 568–580.
86. Giray, C. B.; Dogan, M.; Akalin, A.; Baltrusaitis, J.; Chan, D. C. N.; Skinner, H. C. W.; Dogan, A. U. Sialolith Characterization by Scanning Electron Microscopy and X-ray Photoelectron Spectroscopy. *Scanning* **2007**, *29*, 206–210.
87. Jablonski, A. *Electron Inelastic-Mean-Free-Path Database, 1.1*; National Institutes of Standards and Technology: Gaithersburg, MD, 2000.
88. Beilschmidt, H.; Tiliuin, I. S.; Werner, W. S. M. Inelastic Mean Free-Path of Medium-Energy Electrons in Au, Pt, Ni and Al Determined by Elastic Peak Electron-Spectroscopy. *Surf. Interface Anal.* **1994**, *22*, 120–123.
89. Schmid, G. Nanoclusters–Building Blocks for Future Nanoelectronic Devices? *Adv. Eng. Mater.* **2001**, *3*, 737–743.
90. Cao, L.; Zhu, T.; Liu, Z. Formation Mechanism of Nonspherical Gold Nanoparticles During Seeding Growth: Roles of Anion Adsorption and Reduction Rate. *J. Colloid Interface Sci.* **2006**, *293*, 69–76.
91. Cademartiri, L.; Ozin, G. *Concepts of Nanochemistry*: Wiley-VCH: Weinheim, 2009.
92. Wang, Z. L.; Petroski, J. M.; Green, T. C.; El-Sayed, M. A. Shape Transformation and Surface Melting of Cubic and Tetrahedral Platinum Nanocrystals. *J. Phys. Chem. B* **1998**, *102*, 6145–6151.
93. Dong, Y. Z.; Abaci, S.; Shannon, C.; Bozack, M. J. Self-assembly and Electrochemical Desorption of Thioctic Acid Monolayers on Gold Surfaces. *Langmuir* **2003**, *19*, 8922–8926.
94. Madoz, J.; Kuznetzov, B. A.; Medrano, F. J.; Garcia, J. L.; Fernandez, V. M. Functionalization of Gold Surfaces for Specific and Reversible Attachment of a Fused Beta-galactosidase and Choline-Receptor Protein. *J. Am. Chem. Soc.* **1997**, *119*, 1043–1051.
95. Kuwabata, S.; Fukuzaki, R.; Nishizawa, M.; Martin, C. R.; Yoneyama, H. Electrochemical Formation of a Polyaniline-analogue Monolayer on a Gold Electrode. *Langmuir* **1999**, *15*, 6807–6812.
96. Mazur, M.; Krysinski, P. Covalently Immobilized 1,4-phenylenediamine on 11-Mercaptoundecanoic Acid-coated Gold: Effect of Surface-confined Monomers on the Chemical *in situ* Deposition of Polyaniline and its Derivatives. *Langmuir* **2001**, *17*, 7093–7101.
97. Willey, T. M.; Vance, A. L.; Bostedt, C.; van Buuren, T.; Meulenberg, R. W.; Terminello, L. J.; Fadley, C. S. Surface Structure and Chemical Switching of Thioctic Acid Adsorbed on Au(111) as Observed Using Near-edge X-ray Absorption Fine Structure. *Langmuir* **2004**, *20*, 4939–4944.
98. Porter, M. D.; Bright, T. B.; Allara, D. L.; Chidsey, C. E. D. Spontaneously Organized Molecular Assemblies. 4. Structural Characterization of n-Alkyl Thiol Monolayers on Gold by Optical Ellipsometry, Infrared Spectroscopy, and Electrochemistry. *J. Am. Chem. Soc.* **1987**, *109*, 3559–3568.
99. Schlenoff, J. B.; Li, M.-D.; Ly, H. Stability and Self-exchange in Alkanethiol Monolayers. *J. Am. Chem. Soc.* **1995**, *117*, 12528–12536.
100. Doneux, T.; De Decker, Y. A Simple Model to Describe the Effect of Electrostatic Interactions on the Composition of Mixed Self-Assembeld Monolayers. *Langmuir* **2009**, *25*, 2199–2203.
101. Fawcett, W. R.; Tikanen, A. C. Role of Solvent Permittivity in Estimation of Electrolyte Activity Coefficients on the Basis of the Mean Spherical Approximation. *J. Phys. Chem.* **1996**, *100*, 4251–4255.

102. Fawcett, W. R.; Smagala, T. G. Examination of Ion Size Effects on the Potential Drop Across the Diffuse Layer using Monte Carlo Simulations. *Electrochim. Acta* **2008**, *53*, 5136–5141.
103. Kunze, K. K.; Netz, R. R. Salt-Induced DNA-Histone Complexation. *Phys. Rev. Lett.* **2000**, *85*, 4389–4392.
104. Kamath, G.; Cao, F.; Potoff, J. An Improved Force Field for the Prediction of the Vapor-liquid Equilibria for Carboxylic Acids. *J. Phys. Chem. B* **2004**, *108*, 14130–14136.
105. Akram, M.; Stuart, M. C.; Wong, D. K. Y. Direct Application Strategy to Immobilise A Thioctic Acid Self-assembled Monolayer on a Gold Electrode. *Anal. Chim. Acta* **2004**, *504*, 243–251.
106. Mayya, K. S.; Patil, V.; Sastry, M. On the Stability of Carboxylic Acid Derivatized Gold Colloidal Particles: The Role of Colloidal Solution pH Studied by Optical Absorption Spectroscopy. *Langmuir* **1997**, *13*, 3944–3947.
107. Volkert, A. A.; Subramaniam, V.; Haes, A. J. Implications of Citrate Concentration during the Seeded Growth Synthesis of Gold Nanoparticles. *Chem. Commun.* **2011**, *47*, 478–480.
108. Grabar, K. C.; Freeman, R. G.; Hommer, M. B.; Natan, M. J. Preparation and Characterization of Au Colloid Monolayers. *Anal. Chem.* **1995**, *67*, 735–743.
109. Haiss, W.; Thanh, N. T. K.; Aveyard, J.; Fernig, D. G. Determination of Size and Concentration of Gold Nanoparticles from UV-Vis Spectra. *Anal. Chem.* **2007**, *79*, 4215–4221.
110. Hurst, S. J.; Lytton-Jean, A.; Mirkin, C. A. Maximizing DNA Loading on a Range of Gold Nanoparticle Sizes. *Anal. Chem.* **2006**, *78*, 8313–8318.
111. Usher, C. R.; Baltrusaitis, J.; Grassian, V. H. Spatially Resolved Product Formation in the Reaction of Formic Acid with Calcium Carbonate: The Role of Step Density and Absorbed Water-assisted Ion Mobility. *Langmuir* **2007**, *23*, 7039–7045.